

Single-Bubble Dynamics in Nanopores: Transition Between Homogeneous and Heterogeneous Nucleation

Soumyadeep Paul,¹ Wei-Lun Hsu,¹ Mirco Magnini,² Lachlan R. Mason,³ Ya-Lun Ho,¹ Omar K. Matar,⁴ and Hirofumi Daiguji^{1,*}

¹*Department of Mechanical Engineering, The University of Tokyo 7-3-1, Hongo, Bunkyo-ku, Tokyo 113-8656, Japan*

²*Department of Mechanical Engineering, University of Nottingham, Nottingham, NG7 2RD, United Kingdom*

³*Data-Centric Engineering Programme, The Alan Turing Institute, London, NW1 2DB, United Kingdom*

⁴*Department of Chemical Engineering, Imperial College London, London, SW7 2AZ, United Kingdom*

When applying a voltage bias across a thin nanopore, localized Joule heating can lead to single-bubble nucleation, offering a unique platform for studying nanoscale bubble behavior, which is still poorly understood. Accordingly, we investigate bubble nucleation and collapse inside solid-state nanopores filled with electrolyte solutions and find that there exists a clear correlation between homo/heterogeneous bubble nucleation and the pore diameter. As the pore diameter is increased from 280 nm to 525 nm, the nucleation regime transitions from predominantly periodic homogeneous nucleation to a non-periodic mixture of homogeneous and heterogeneous nucleation. A transition barrier between the homogeneous and heterogeneous nucleation regimes is defined by considering the relative free-energy costs of cluster formation. A thermodynamic model considering the transition barrier and contact-line pinning on curved surfaces is constructed, which determines the possibility of heterogeneous nucleation. It is shown that the experimental bubble generation behavior is closely captured by our thermodynamic analysis, providing important information for controlling the periodic homogeneous nucleation of bubbles in nanopores.

Keywords: Ionic Joule heating, Solid-state nanopores, Periodic bubble generation, Seed bubbles, Microchannel heat sink, Hetero/homo bubble nucleation, Cluster ripening

I. INTRODUCTION

Following Moore's Law, transistors continue to shrink, enabling the miniaturization of electronic chips. In the meantime, these closely packed electronic components are subject to significant heat generation in high-performance electronic devices. In this context, two-phase cooling using microchannel evaporators has emerged as an energy-efficient cooling solution. In this system, liquid refrigerant enters from one end of a channel and vaporizes while consuming heat from the underlying chip. However, this heat transfer method via flow boiling may cause chip overheating due to flow instabilities originating from spontaneous bubble nucleation on the channel walls. Although previous studies have shown that boiling incipience and its associated instabilities could be effectively eliminated through wall nucleation suppression and microheater bubble seeding [1–3], controlling the unpinning and departure dynamics of heterogeneous (hetero) nucleating bubbles from the heater surfaces remains challenging. For compact systems (e.g., 3D chips) comprising sub-100- μm channels, homogeneous (homo) bubble seeds, originating in the bulk phase and operating on the nanoscale, are needed.

Homogeneous nanobubble [4, 5] generation inside nanopores can serve as a potential method for bubble seeding. Through the application of a high-voltage bias across a solid-state nanopore immersed in a concentrated salt solution, intense and localized Joule heat is produced

inside the nanopore. After the initial heating, the solution inside the nanopore becomes metastable, following which a bubble nucleates homogeneously under a superheating condition.

Golovchenko and coworkers [4, 5] showed that homo nucleation inside the nanopore leads to periodic and uniformly sized nanobubbles, making it attractive for generation of a well-organized succession of bubbly, slug, and annular flow regimes in microchannels. Not only do these homo nanopore bubbles hold tremendous potential for electronic cooling [2], but they could also play a role in various applications ranging from biomedical imaging [6] to froth flotation [7]. However, depending on conditions, hetero bubble nucleation, which requires a lower nucleation energy [8, 9], can simultaneously occur on the inner walls of the nanopore, reducing the efficiency of homo bubble emission. Despite the fact that bubble nucleation on metallic nanoparticles [9], nanorods [10], and nanodots [11] has gained significant attention in recent years due to its potential game-changing applications in photothermal cancer therapy [12] and solar thermal powerplants [13, 14], the exact mechanisms of homo/hetero nucleation and pinning or confinement effects are still under debate, and an in-depth understanding is lacking.

In this paper, we investigate the bubble generation mechanism in nanopores due to Joule heating effects to control the occurrence of homo and hetero bubble nucleation. We study bubble generation in 280-nm and 525-nm nanopores (Fig. 1) and show that in the smaller pores, homo nucleation is dominant, giving rise to periodic bubbles, while the bigger pores yield a combination of homo and hetero bubbles, eliminating the periodicity.

* Corresponding author: daiguji@thml.t.u-tokyo.ac.jp

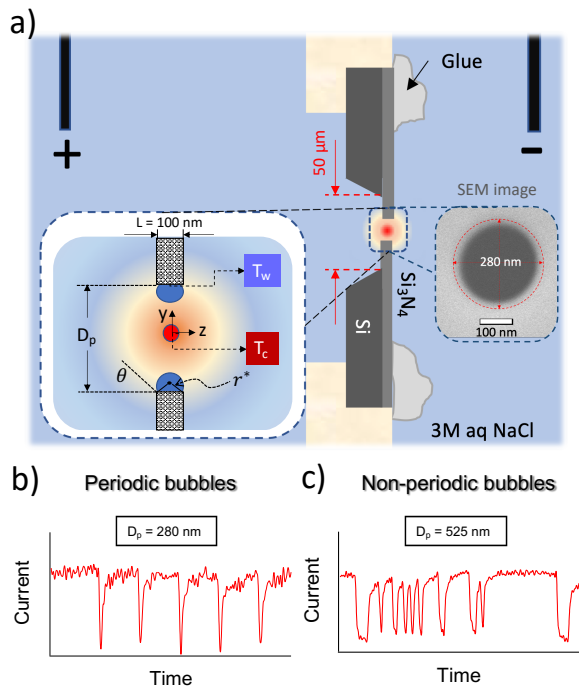


FIG. 1. (a) Schematic of nanopore bubble generation. Left inset: homo and hetero cluster formation at pore center and pore walls; right inset: SEM image of $D_p = 280$ nm nanopore. (b) Uniform quasi-periodic signals are observed when there is only homo nucleation. (c) Periodicity is lost when hetero nucleation starts at pore walls.

We introduce a thermodynamic parameter, the transition barrier (ξ), to elucidate the transition dynamics between homo and hetero bubble nucleation. In addition to ξ , a second parameter of interest, ζ , is established that captures the effect of nanoconfinement due to limited available surface area for hetero nucleation on the surface of the pore walls. Both these parameters influence the contact angle and the nucleation temperature of the hetero bubbles. This study will shed light on the transition mechanism between homo and hetero nucleation.

II. EXPERIMENTAL METHODS

Circular nanopores (as seen in the scanning electron microscope (SEM) image shown in the right inset of Fig. 1(a) and Supplemental Material Fig. S1.1 [15]) were made on silicon nitride chips purchased from Alliance Biosystems Inc., each comprising a 100-nm-thick silicon nitride (Si_3N_4) membrane deposited on a 200- μm -thick silicon substrate with an approximately square $50\ \mu\text{m} \times 50\ \mu\text{m}$ opening at the center. The nanopores were etched at the center of the free-standing part of the membrane using a focused ion beam (SMI3050: SII Nanotechnology, a precisely focused “fine” Ga^+ beam at around 10–17 pA). Before performing the experiments, the nanopore-containing chip was boiled in a piranha so-

lution to remove organic contaminants. The chip was then glued between two additively manufactured fluidic tanks such that the nanopore became the only fluidic connection [Fig. 1(a)], and these fluidic tanks were filled with 50% ethanol solution to ensure that there were no air gaps in the nanopore system. A 3M NaCl electrolyte solution was prepared by diluting 5M NaCl (Sigma-Aldrich) with deionized (DI) water. Before transferring the electrolyte into the fluidic tanks, they were flushed with DI water multiple times, followed by flushing with 3M NaCl multiple times to remove any traces of ethanol or water in the system. After these steps, the fluidic tanks were filled with the prepared 3M NaCl solution. Ag/AgCl electrodes were inserted into the tanks, and square voltage pulses were applied across the nanopore by means of a function generator (Tektronix AFG3151C). The circuit current was determined by measuring the voltage across a shunt resistor using a high-bandwidth oscilloscope (Tektronix MDO3052). Downward current spikes were observed when bubbles were generated, blocking ion transport through the nanopore. Analysis of the nucleation time and bubble duration based on current variations revealed the nucleation conditions and bubble behavior in the nanopore. For the pore configurations considered in this study, a 3%–4% increase in the baseline current over time for a given bias voltage was observed due to minor expansion of the pore diameter [16].

III. THEORETICAL ANALYSIS

Due to the high magnitude of the bias voltages and the small thickness of the dielectric membrane, an intense electric field was generated in the nanopore, which was converted into remarkable Joule heat (H) following $H = \mathbf{J} \cdot \mathbf{E}$. Here, $\mathbf{J} = \sigma \mathbf{E}$ is the current density when the advection current is negligible; \mathbf{E} is the local electric field, and σ is the ionic conductivity. This Joule heat is transferred to the surrounding electrolyte as well as to the silicon nitride membrane, resulting in a sharp thermal gradient in the vicinity of the membrane wall in the solution. As the nanopore Joule heating progresses, the pore center temperature, T_c rises at a higher rate than the wall temperature, T_w , leading to $T_c > T_w$ (Fig. 1). Prior to the Joule-heating process, $T_c = T_w = T_0$, where T_0 is the ambient temperature.

Unlike previous studies on microheater bubbles [17–19] where the bulk temperature is always lower than the surface temperature, thereby allowing only hetero nucleation, in nanopore Joule heating, a higher liquid temperature at the pore center also allows the possibility of homo nucleation. For homo nucleation, a higher superheating temperature is required to satisfy the kinetic requirement for cluster formation ($T_c > 575$ K for water [20]), whereas hetero nucleation temperatures largely depend upon the dimensions of the nanostructures on the nucleating surface, following the Young–Laplace equation [8] (424 K

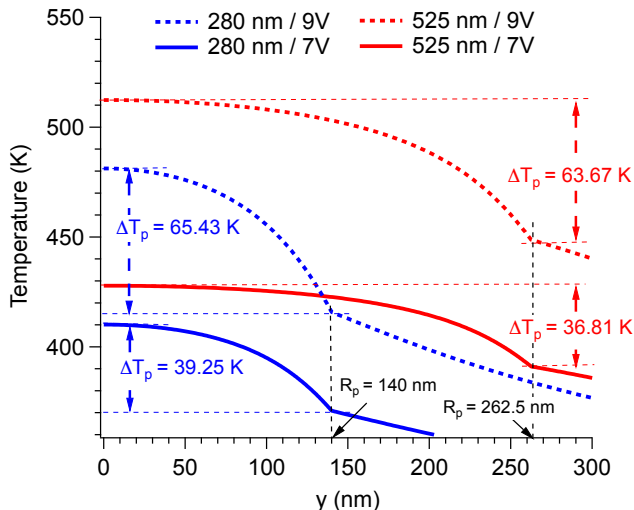


FIG. 2. Temperature distribution across pore cross-section for $D_p = 280$ nm and 525 nm after $20 \mu\text{s}$ of Joule heating under bias voltages of 7 V and 9 V, with $T_0 = 300.15$ K. The x axis denotes the radial position from the pore centerline, as shown in Fig. 1(a), left inset. $R_p = D_p/2$ is the pore radius. The value of σ in Eq. (1) was defined at T_0 , which remained constant during the simulation.

to 474 K for decreasing nanostructure diameters from 500 nm to 100 nm).

The cross-pore radial temperature difference, expressed as $\Delta T_p = T_c - T_w$, dictates whether nanopore Joule heating will result in a homo or hetero bubble. ΔT_p can be controlled by varying the pore diameter and bias voltage. To obtain the temperature distribution responsible for the bubble behavior, numerical simulations were employed to solve the energy-conservation equation

$$\rho c_p \frac{\partial T}{\partial t} = \frac{1}{y} \frac{\partial}{\partial y} \left(\kappa y \frac{\partial T}{\partial y} \right) + \frac{\partial}{\partial z} \left(\kappa \frac{\partial T}{\partial z} \right) + \sigma |\mathbf{E}|^2, \quad (1)$$

where ρ , c_p , and κ denote the temperature-dependent water density, specific heat, and thermal conductivity, respectively, and t represents time. On an axisymmetric reference frame centered at the center of the nanopore, y represents the radial coordinate and z the axial coordinate. Equation (1) was solved on a finite-volume mesh with appropriate boundary conditions and numerical discretizations (Supplemental Material, Sec. 2 [15]).

Figure 2 shows the simulated nanopore cross-sectional temperature distributions for pores of $D_p = 280$ nm and 525 nm obtained after $20 \mu\text{s}$ of Joule heating for bias voltages of 7 V and 9 V. We can draw two major observations: i) a higher voltage leads to a higher temperature rise and higher ΔT_p ; and ii) for the same voltage, a smaller pore results in a higher value of ΔT_p ($\Delta T_{p280} - \Delta T_{p525}$ is 2.44 K and 1.76 K for $V_{\text{app}} = 7$ V and $V_{\text{app}} = 9$ V, respectively). It should be noted that, for simplicity, we neglected the effect of temperature on

the electrical conductivity in this section. In the complete Joule-heating model, as explained in the Supplemental Material, Sec. 1 [15], σ increases with T , following an empirical relationship established in a previous study [5]. For our pore and voltage configurations, we tuned this σ - T relationship to fit the experimentally observed nanopore current in our simulations (Supplemental Material, Secs. 2 and 3 [15]). In future sections, we incorporate this relationship into the Joule-heating model to capture the nanopore temperature distributions. As $T_c > T_w$, when the σ - T variation is considered, a greater amount of Joule heat would be generated at the pore center than at the pore walls, resulting in an even higher ΔT_p . The transient variations of T_c and T_w for the pore configurations under study are shown in the Supplemental Material, Sec. 4 [15].

The average electric field magnitude inside the nanopore can be approximately obtained from the nanopore circuit model [21] as

$$E_p = \frac{V_{\text{app}}}{\left(L + \frac{\pi D_p}{4}\right)}, \quad (2)$$

where L is the membrane thickness (pore length). Equation (2) shows that when increasing the bias voltage, V_{app} , and decreasing the pore diameter, D_p , the electric field within the nanopore intensifies, causing more intense Joule heating. If we consider a uniform electric field within the nanopore and neglect the temperature dependency of the thermophysical quantities and diffusion in the z direction, the radial temperature difference across the nanopore, ΔT_p , can be expressed as

$$\Delta T_p(t) = D_T \int_0^t [\nabla^2(T_c - T_w)] dt, \quad (3)$$

where $\nabla^2 = \frac{1}{y} \frac{\partial}{\partial y} \left(y \frac{\partial}{\partial y} \right)$ is the y component of the Laplacian operator, T_c and T_w denote the nanopore temperatures near the pore center and pore walls, respectively, and $D_T = \kappa/\rho c_p$ denotes the thermal diffusivity. In a steady state, $\nabla^2 T_c = \nabla^2 T_w$, but during the transient heating, $0 > \nabla^2 T_c > \nabla^2 T_w$, ensuring that $\Delta T_p > 0$, and this increases with time.

A. Thermodynamics of nucleation

1. Energetics of cluster formation

Due to ionic Joule heating, the liquid confined inside the nanopore enters a metastable state, and vapor cluster (or embryo) groups originate at the pore walls and center [Fig. 6(a)]. These clusters are aggregates of vapor molecules that form and shrink spontaneously in the metastable liquid. Cluster formation from the bulk metastable liquid requires a minimum (reversible) work W . For a cluster having a critical radius r^* and containing a critical number of molecules n^* , W reaches a maximum value. Clusters having a larger number of molecules

than this cluster will grow spontaneously as the free energy decreases [22]. $W(n^*)$ decreases as the superheating is increased, making it easier for a critical cluster to appear. The reversible work needed for the formation of a spherical vapor cluster of radius r in the bulk liquid is given by [22]

$$W_{\text{ho}}(r, P_v) = \left[4\pi r^2 \gamma - \frac{4}{3} \pi r^3 (P_v - P) + \frac{4}{3} \pi r^3 P_v \ln \frac{P_v}{P_v^*} \right] \quad (4)$$

in which the superscript ‘*’ denotes the properties of a critical-sized cluster. In this equation, P is the atmospheric pressure, P_v is the vapor pressure inside the bubble, and γ is the surface tension at the cluster interface, which is evaluated at the cluster temperature, T_v .

The vapor pressure of the critical cluster, P_v^* , is related to the saturation vapor pressure, P_{sat} and the critical cluster temperature, T_v^* according to $P_v^* = P_{\text{sat}} \exp[(P - P_{\text{sat}})M_w / (N_A \rho k T_v^*)]$. Here, P_{sat} and the liquid density ρ are evaluated at T_v^* assuming saturation conditions. M_w , N_A , and k denote the molecular weight of water, Avogadro’s number, and Boltzmann’s constant, respectively. Assuming the critical cluster to be in thermal equilibrium with the liquid surrounding it [23], T_v^* is calculated according to

$$\kappa \iint_{S_b} \frac{(T - T_v^*)}{\delta_\delta} dS = 0, \quad (5)$$

where T is the liquid temperature inside the pore obtained from the Joule heating simulations and interpolated over the liquid–vapor interface of the bubble, S_b . We assume a linear temperature gradient across a uniform thermal boundary-layer thickness, δ_δ at S_b . Assuming the critical cluster to be in mechanical equilibrium, P_v^* is related to the cluster radius through the Young–Laplace equation

$$P_v^* = P + \gamma^* K, \quad (6)$$

where K is the curvature of the bubble surface, which for a spherical homo bubble is given by $K = 2/r^*$. As P_v^* and γ^* are both temperature-dependent properties, we can express the critical radius r^* as a function of its temperature, which is shown by the blue curve in Fig. 3(a). Conversely, through Eq. (5) we can express the vapor temperature of clusters of various sizes located at the pore center given the liquid temperature distribution at any given time [Fig. 3(a)]. The critical points [marked by circles in Fig. 3(a)] where these two curves intersect give us the solutions for the radius and temperature of critical clusters where both Laplace and thermal equilibrium are satisfied. In our model, we assume that all cluster sizes have the same pressure and temperature as a critical cluster, i.e., $P_v = P_v^*$ and $T_v = T_v^*$. This means that they have the same chemical potential. The free energy

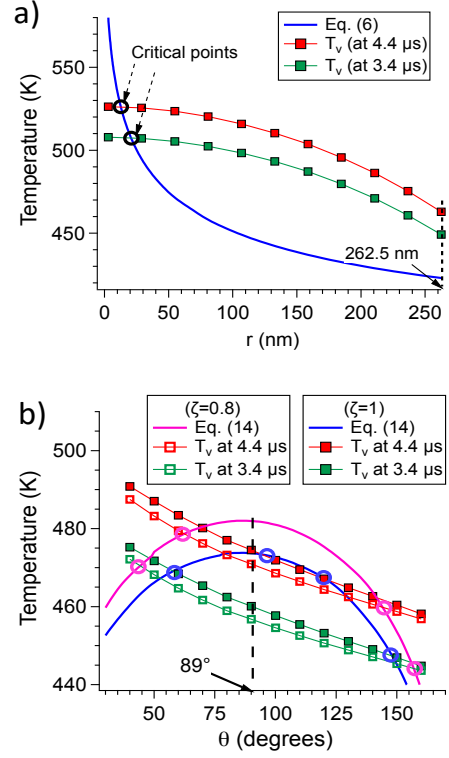


FIG. 3. Variation of cluster temperature with size according to Laplace equilibrium (solid line) and thermal equilibrium (line with markers) for (a) homo bubbles having radius r , and (b) hetero bubbles having $\zeta = 1$ and $\zeta = 0.8$ inside a $D_p = 525$ nm pore. The solid and hollow square markers show the variations of vapor temperature inside bubbles having $\zeta = 1$ and $\zeta = 0.8$, respectively, when they are in thermal equilibrium with the superheated liquid inside the pore for specific time points [Eq. (5)]. The liquid temperature distribution was evaluated through Joule-heating simulations for $V_{\text{app}} = 7.08$ V across a $D_p = 525$ nm pore. The round hollow markers indicate the points where both Laplace and thermal equilibrium are satisfied, indicating the size and temperature inside a critical nucleus.

of a homo cluster can be expressed as

$$W_{\text{ho}}(n) = 4\pi\gamma^* \left(\frac{3kT_v^* n}{4\pi P_v^*} \right)^{\frac{2}{3}} - nkT_v^* \left(1 - \frac{P}{P_v^*} \right), \quad (7)$$

where n is the number of molecules inside the cluster, and according to ideal gas law, this is given by

$$n = \frac{P_v V_b}{kT_v} \approx \frac{P_v^* V_b}{kT_v^*}, \quad (8)$$

where V_b is given by

$$V_b = \begin{cases} \frac{4}{3} \pi r^3, & \text{for a homo cluster} \\ \frac{\pi}{3} r^3 f(\theta), & \text{for a hetero cluster} \end{cases} \quad (9)$$

where $f(\theta) = 2 + 3 \cos(\theta) - \cos^3(\theta)$ and θ represents the contact angle formed by the bubble at the vapor–solid

interface on the liquid side, as shown in Fig. 1(a) (left inset). For hetero bubble nucleation on circular pore walls, we can express the reversible work for cluster formation as

$$W_{\text{he}}(r, \theta) = \gamma^* \pi r^2 \left[f(\theta) + \varepsilon \frac{\sin^4(\theta)}{4} \right] - \frac{\pi}{3} r^3 (P_v^* - P) f(\theta). \quad (10)$$

Here, the first term corresponds to the free energy associated with the creation of the bubble surface and the second term is associated with the volume contribution. Due to the curvature of the pore walls, the shape of the bubble becomes distorted from the equilibrium shape of a spherical cap on a flat surface. Here, $\varepsilon = -r/R_p$ is the perturbation parameter associated with the deformed surface. Soleimani *et al.* [24] approximately solved for the bubble/drop shape on a cylindrical surface in the absence of gravity by perturbing a spherical cap on a flat surface subject to the constraints of constant volume, uniform interface curvature, and the validity of the Young–Dupré condition at the contact line. The term $\varepsilon \frac{\sin^4(\theta)}{4}$ in Eq. (10) captures the perturbation in the surface energy due to the curvature of the nucleating surface, which decreases with increasing pore diameter and vanishes completely for a flat surface, in which case, $R_p \rightarrow \infty$. Although, only the first-order solution with respect to the perturbation parameter ε was considered, Soleimani *et al.* [24] were able to show a good match of interface surface area and curvature when compared with numerical solutions, even when $|\varepsilon| \rightarrow 1$ for large values of $|\theta - 90^\circ|$. As $\theta \rightarrow 90^\circ$, the error increases, particularly for higher values of ε . For example, the error in the perturbation surface free-energy term was shown to increase to $\sim 21\%$ at $\theta = 90^\circ$ when $\varepsilon = 0.5$ [24].

Substituting r by n in Eq. (10) by combining Eqs. (8) and (9), we arrive at

$$W_{\text{he}}(n, \theta) = \pi \gamma^* \left(\frac{3kT_v^* \sqrt{f(\theta)}}{\pi P_v^*} \right)^{\frac{2}{3}} n^{\frac{2}{3}} - \frac{nkT_v^*}{P_v^*} \left(P_v^* - P + \frac{3\gamma^* \sin^4(\theta)}{4R_p f(\theta)} \right). \quad (11)$$

Here, the vapor pressure of a critical hetero cluster, P_v^* , is given by Eq. (6), where the mean curvature K is given by [24]

$$K = \frac{\{2 + [3\varepsilon \sin^4(\theta)]/[4f(\theta)]\}}{r^*}. \quad (12)$$

In this equation, P_v^* increases with the vapor temperature T_v^* , while γ^* decreases with T_v^* . Interestingly, when we try to find the critical point by taking $\partial W_{\text{he}}/\partial r = 0$ in Eq. (10), we arrive at the same Laplace condition given by Eqs. (6) and (12). Similar to the perturbation surface

free energy, the error in K also increases as $\theta \rightarrow 90^\circ$, particularly for high values of $|\varepsilon|$. For $\varepsilon = -0.9$, an error of $\sim 18\%$ in K was found with respect to the numerical simulations for $\theta = 90^\circ$.

For higher values of K , the required nucleation temperature T_v^* would be higher [Eq. (6)]. Also, as $\varepsilon < 0$ for a concave surface, the bubble curvature is lower than that for a flat surface for the same contact angle.

Unlike homo nucleation, hetero nucleation is constrained by the available nanostructure area [8]. So, for a given contact angle, let the liquid–vapor interface of the bubble be given by $z_1 = z_1(a, \phi)$. Here, the bubble surface is expressed in axisymmetric co-ordinates about the bubble axis [shown in Fig. 4, inset (a)]. The parameter a is a radial co-ordinate and z_1 is the axial distance from the bubble’s center of curvature. Both a and z_1 are non-dimensionalized with respect to the bubble radius r . More details about the bubble shape are provided in the Supplemental Material, Sec. 5 [15]. Now, for the $\phi = 90^\circ$ plane, which cuts the pore surface in a straight line, the radial distance of the intersection point of the bubble and the pore surface a_i is given by imposing the condition $z_1(a_i, \phi = 90^\circ) = \cos(\theta)$. Then, a_i becomes a function of θ , which for a flat surface is given by $a_i = \sin(\theta)$.

For a given θ , $2a_i r^* = L$ is now the maximum coverage of the pore walls along the $\phi = 90^\circ$ plane that a hetero bubble can have. In other words, the geometry of the pore imparts a constraint on the bubble size

$$\zeta(r, \theta) = \frac{2a_i(\theta)r}{L} \Rightarrow \zeta \leq 1, \quad (13)$$

where ζ represents the fraction of the pore length covered by the hetero bubble. As the hetero bubble must fit on the pore walls, ζ should always be less than or equal to 1.

Subject to mechanical equilibrium according to the Laplace equation, the nucleation temperature as a function of contact angle can be deduced as

$$P_v^* = P + \gamma^* \left(\frac{4a_i(\theta)}{\zeta L} - \frac{3 \sin^4(\theta)}{4R_p f(\theta)} \right). \quad (14)$$

We obtain the size and temperature of the critical nucleus [marked by hollow circles in Fig. 3(b)] by solving for the roots of Eqs. (14) and (5). The Laplace equilibrium curve is shown by the blue and pink lines for $\zeta = 1$ and $\zeta = 0.8$, respectively. We find that with decreasing ζ , the Laplace equilibrium curve shifts upwards, while the thermal equilibrium curve shifts downwards, causing their roots to move away from each other.

At $\zeta = 1$, for a given θ , n^* is the number of molecules inside a critical cluster ($r = r^*$), which is given by solving Eqs. (8) and (14). For any value of θ , when $n < n^*$, the bubble will always satisfy $\zeta < 1$. However, further addition of molecules to the critical cluster at $\zeta = 1$ results in pinned growth, during which the contact angle θ should reduce such that the constraint of $\zeta = 1$ is maintained [as shown in Fig. 4, inset (b)]. During this stage, the bubble

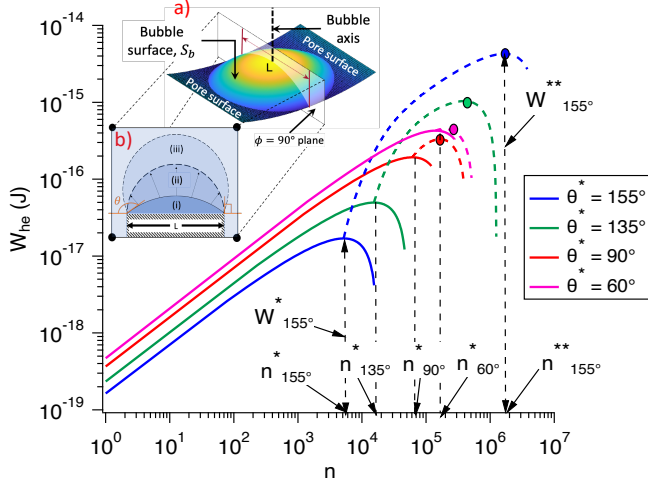


FIG. 4. Solid and dotted lines showing the computed reversible work for hetero cluster formation during unpinning and pinned bubble growth according to Eqs. (11) and (14) for $\zeta = 1$ on $D_p = 525$ nm pore. Inset (a) shows the 3D shape of a $\zeta = 1$ hetero bubble having $\theta = 135^\circ$ on a $D_p = 525$ nm pore. Inset (b) shows the pinned growth of a surface nanobubble after $n = n^*$.

radius varies as

$$r(\theta) = \frac{L}{[2a_i(\theta)]}. \quad (15)$$

Thus, unlike the unpinning stage, during the pinned stage, r and θ are not independent and are related through Eq. (15). Consequently n and W_{he} are given by combining Eq. (15) with Eqs. (8) and (10), respectively. Figure 4 shows the variation of W_{he} during unpinning growth from $n = 1$ to $n = n^*$ when $\theta = \theta^*$ by solid lines and pinned growth for $n > n^*$ during which $\theta < \theta^*$ by dotted lines. Here, θ^* denotes the contact angle of a critical cluster. During the unpinning stage, a local maximum of free energy W_{he} is observed at $n = n^*$. $W_{he} = W_{he}^*$ at $n = n^*$. The general expression for W_{he}^* is given by

$$W_{he}^*(\zeta, \theta) = \frac{\pi\gamma^*L^2\zeta^2f(\theta)}{12a_i^2}. \quad (16)$$

As the term $f(\theta)/a_i^2$ decreases monotonically with θ , W_{he}^* decreases with increasing θ^* , as shown in Fig. 4. For homo nucleation, the free energy of critical cluster depends only upon the critical cluster radius, however for hetero nucleation, the critical free energy depends upon two shape parameters, ζ and θ . Without contact-line pinning, W_{he}^* would have been the net free-energy barrier for hetero nucleation. However, due to the pinning effect, the reversible work increases beyond $n = n^*$ until $n = n^{**}$, at which point a second maximum of W_{he} is observed. Here, the superscript ‘**’ represents the second critical point, which is reached during pinned growth. $W_{he} = W_{he}^{**}$ and $\theta = \theta^{**}$ at $n = n^{**}$. For pinned hetero nucleation on a flat surface, we can easily solve for θ^{**}

by solving for $\left|\frac{dW_{he}}{d\theta}\right|_{\theta=\theta^{**}} = 0$, where W_{he} is given by Eq. (10), such that

$$\begin{aligned} \pi\gamma^*L^2 \left[\frac{d}{d\theta} \left(\frac{f(\theta)}{4\sin^2\theta} - \frac{f(\theta)\sin(\theta^*)}{6\sin^3\theta} \right) \right] &= 0 \\ \Rightarrow 3\sin^5(\theta^{**}) + 4\sin(\theta^{**})\cos(\theta^{**}) & \\ + 6\sin(\theta^{**})\cos^2(\theta^{**}) - 2\sin(\theta^{**})\cos^4(\theta^{**}) & \\ = 2\sin(\theta^*)\sin^4(\theta^{**}) + 4\sin(\theta^*)\cos(\theta^{**}) & \\ + 6\sin(\theta^*)\cos^2(\theta^{**}) - 2\sin(\theta^*)\cos^4(\theta^{**}). & \quad (17) \end{aligned}$$

Now, for θ much greater than 90° , $\theta^{**} \approx 180^\circ - \theta^*$ will be the solution to Eq. (17), as $\sin^5(\theta^*) \approx 0$ and can be neglected compared to the other terms [Fig. 5(c)]. Additionally, for a flat surface, the T_v^* versus θ^* curve is symmetric about $\theta = 90^\circ$ [Fig. 5(b)], i.e., $T_v^*(\theta^*) = T_v^*(\theta^{**})$. So, Laplace equilibrium is satisfied at both $\theta = \theta^*$ and $\theta = \theta^{**}$. Also, $W_{he}^{**}(\theta^*) = W_{he}^*(180^\circ - \theta^*)$. Thus, for $\theta_1 < \theta_2$, where both angles are much greater than 90° , $W_{he}^{**}(\theta_2) > W_{he}^{**}(\theta_1)$ as $W_{he}^*(180^\circ - \theta_2) > W_{he}^*(180^\circ - \theta_1)$, as per Eq. (16).

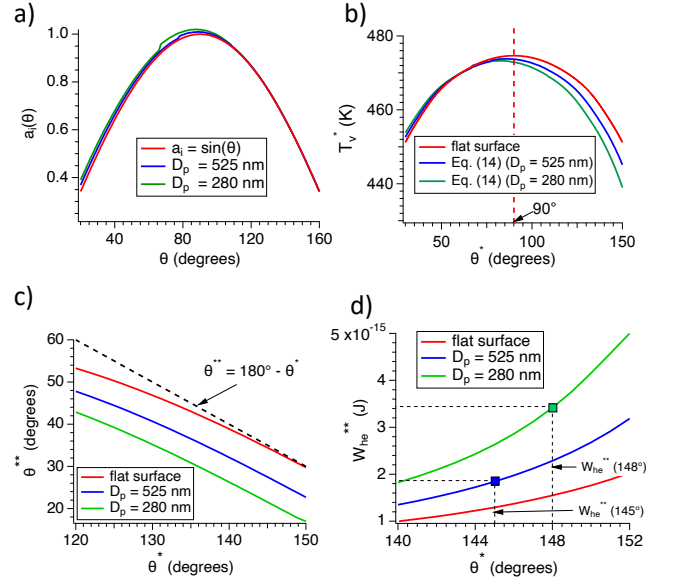


FIG. 5. Variation of (a) a_i and (b) vapor temperature inside a bubble with θ subject to the Laplace equation for $\zeta = 1$. Variation of (c) W_{he}^* and (d) W_{he}^{**} with θ^* for a $\zeta = 1$ hetero bubble.

In comparison to a flat surface, for a bubble on a curved surface having θ^* much greater than 90° , T_v^* is lower due to a reduction in bubble curvature following Eq. (14) [Fig. 5(b)]. As a result, the corresponding value of θ^{**} for which Laplace equilibrium is re-established during pinned growth would be $\theta^{**} < 180^\circ - \theta^*$, as seen in Fig. 5(c). Furthermore, as W_{he}^* increases with decreasing θ^* , this indicates that W_{he}^{**} increases with decreasing pore diameter for a given θ^* , as shown in Fig. 5(d).

This analysis also indicates that the more obtuse the bubble contact angle at the critical point, the higher the net free-energy barrier W_{he}^{**} . This can be noticed in

both Figs. 4 and 5(d). Thus, although a critical nucleus having n^* molecules is in Laplace and mechanical equilibrium, it has to overcome an additional free-energy barrier, $W_{\text{he}}^{**} - W_{\text{he}}^*$, to reach spontaneous growth conditions. Also, for a given value of θ^* , the additional free-energy barrier is higher for smaller pores, making hetero bubble growth comparatively more difficult than for bigger pores. This model indicates that, due to contact-line pinning, although hetero nucleation is easier at higher contact angles, it also requires a higher additional free-energy barrier to reach the spontaneous growth conditions. A similar conclusion was reached in a previous study [25], where obtuse contact-angled nanobubbles were shown to form more easily than their acute-angled counterparts, although the former were difficult to destabilize for nucleation. It is likely that in our system, high contact-angle surface nanobubbles may nucleate on pore walls, but they either fail to or very rarely grow to completely block the nanopore due to the pinning effect.

2. Cluster-group competition

When the liquid inside a pore is sufficiently superheated, both homo and hetero clusters will appear, and, depending upon their relative free-energy requirements, a competition is expected to originate between these two cluster groups.

In the literature, Ostwald ripening of bubbles has been studied, which relates to the evolution of bubble size distributions post-nucleation. When a distribution of bubble sizes is formed after nucleation in an infinite medium, the larger bubbles grow at the expense of the smaller bubbles so as to reduce the total surface free energy [26–30]. In this study, we employ a similar concept to vapor clusters originating prior to the nucleation point. During the initial range of superheating, when the pore liquid is in a metastable state but far from critical conditions, a competition may occur between the cluster groups at the pore walls and center. If we consider both cluster groups as a single system and assume reversible work for cluster formation (i.e., work recovered from the collapse of either cluster group would be utilized for growth of the other group), growth of the cluster group requiring a lower W would be favored. To the best of our knowledge, competition between homo and hetero cluster groups has not previously been studied. As the temperature increases inwards from the pore walls, the free-energy cost of homo clusters can become comparable to that of hetero cluster formation. This allows the possibility of such a competition. In the traditional case of hetero nucleation, where the heat flows from the surface to the liquid, liquid near the surface would always have a higher temperature than the bulk and accordingly hetero clusters would be associated with a lower free-energy cost.

We hypothesize that the cluster ripening equilibrium [Fig. 6(a)] would shift towards the cluster group that would require a lower free-energy work per molecule of

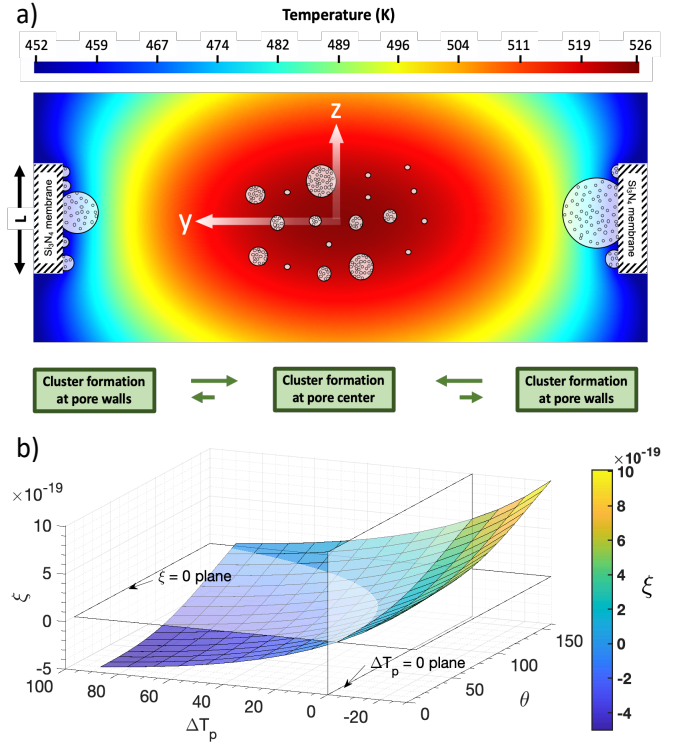


FIG. 6. (a) Schematic explanation of vapor cluster formation inside a nanopore. The temperature contour corresponds to the temperature distribution at 4.4 μs , which was obtained through a simulation of Joule heating for 7.08 V applied across a $D_p = 525$ nm pore. (b) Variation of ξ with ΔT_p and θ for $D_p = 525$ nm pore. Here, $T_w = 460\text{K}$ and $T_c = T_w + \Delta T_p$. The homo and hetero clusters are at T_c and T_w , respectively.

addition. This means that if the group of hetero clusters would require a higher free-energy work to grow by ΔN molecules than the group of homo clusters for the same number of molecules, then the homo cluster group would grow at the expense of the loss of molecules from the hetero clusters. In such a scenario, there is a possibility that even if the hetero clusters reach conditions very close to the critical conditions, the equilibrium could shift back to homo cluster ripening, thereby suppressing hetero nucleation. To study this phenomenon quantitatively, we calculate X , which is defined as the total free energy of either cluster group, such that

$$X_{\text{ho}} = \sum_{n=1}^{n^*} M_{\text{ho}} W_{\text{ho}}(n) \exp\left(-\frac{W_{\text{ho}}(n)}{kT_v^*}\right)$$

$$X_{\text{he}}(\theta) = \sum_{n=1}^{n^*} M_{\text{he}}(\theta) W_{\text{he}}(n, \theta) \exp\left(-\frac{W_{\text{he}}(n, \theta)}{kT_v^*}\right), \quad (18)$$

Here T_v^* for homo and hetero clusters are obtained from the solution of Laplace and thermal equilibrium curves [Fig. 6(a,b)]. The total number of molecules in either

group is given by

$$N_{\text{ho}} = M_{\text{ho}} \sum_{n=1}^{n^*} n \exp\left(-\frac{W_{\text{ho}}(n)}{kT_v^*}\right)$$

$$N_{\text{he}}(\theta) = M_{\text{he}}(\theta) \sum_{n=1}^{n^*} n \exp\left(-\frac{W_{\text{he}}(n, \theta)}{kT_v^*}\right). \quad (19)$$

Here, M_{ho} and $M_{\text{he}}(\theta)$ are the total numbers of clusters in the homo and hetero cluster groups having contact angle θ , respectively. We assume here that clusters belonging to either group will follow a Boltzmann distribution. As the free energy of the clusters increases with size, the number of clusters decays exponentially. As a result, the quantity X depends remarkably upon the free energies of the smaller cluster sizes belonging to each group. Now, if each cluster group is provided with ΔN additional molecules, let the change in the number of clusters of the homo and hetero groups be given by M'_{ho} and $M'_{\text{he}}(\theta)$, respectively. It follows that

$$\Delta N = M'_{\text{ho}} \sum_{n=1}^{n^*} n \exp\left(-\frac{W_{\text{ho}}(n)}{kT_v^*}\right)$$

$$= M'_{\text{he}}(\theta) \sum_{n=1}^{n^*} n \exp\left(-\frac{W_{\text{he}}(n, \theta)}{kT_v^*}\right), \quad (20)$$

and the free-energy cost associated with extra cluster formation is given by

$$\Delta X_{\text{ho}} = M'_{\text{ho}} \sum_{n=1}^{n^*} W_{\text{ho}}(n) \exp\left(-\frac{W_{\text{ho}}(n)}{kT_v^*}\right)$$

$$\Delta X_{\text{he}}(\theta) = M'_{\text{he}}(\theta) \sum_{n=1}^{n^*} W_{\text{he}}(n, \theta) \exp\left(-\frac{W_{\text{he}}(n, \theta)}{kT_v^*}\right). \quad (21)$$

The relative specific free-energy cost for cluster population growth can be expressed as

$$\xi = \frac{\Delta X_{\text{ho}}}{\Delta N} - \frac{\Delta X_{\text{he}}(\theta)}{\Delta N}. \quad (22)$$

When $\xi < 0$, the specific free-energy cost of hetero cluster formation is higher than that of homo cluster formation. As the equilibrium between the two cluster groups would shift in the direction having a lower specific free-energy cost, $\xi < 0$ would indicate that homo clusters would increase in population while hetero clusters would shrink back to the liquid phase. As the total cluster population decreases, the number of critically sized clusters decreases proportionally, reducing the statistical feasibility of hetero nucleation. The parameter ξ essentially depends upon the vapor temperatures of the clusters in the homo and hetero groups and also the contact angle θ of the hetero group.

Figure 6(b) summarizes the impact of θ and ΔT_p on ξ . The hetero clusters originating at the pore walls are

assumed to be at T_w , while the homo clusters originating at the pore center are assumed to be at T_c . We find that ξ increases with decreasing ΔT_p and increasing θ . With increasing temperature, the free-energy cost for cluster formation reduces, hence when T_c is greater than T_w , it is possible that the relative free-energy cost for homo cluster formation can be lower than for hetero cluster formation. On the other hand, the free-energy barrier for hetero nucleation decreases with θ [Eq. (16)], which causes ξ to increase with increasing θ . When $\Delta T_p < 0$, $\xi > 0$ for all θ , which makes the suppression of hetero nucleation impossible [Fig. 6(b)]. For $\Delta T_p > 0$, there exist $\theta - \Delta T_p$ ranges where $\xi < 0$, thereby signifying possible suppression of hetero nucleation. In the previous subsection, we showed that at a given time point, there are two solutions for the contact angle for which Laplace and thermal equilibrium are satisfied [Fig. 3(b)]. For the lower solution value of θ , although ΔT_p is lower than ΔT_p for the higher solution value of θ , it is still high enough to fall into the $\xi < 0$ region. As a result, in most cases, it is expected that hetero nucleation would be suppressed for the lower solution value of θ .

IV. RESULTS AND DISCUSSION

We have observed bubble nucleation and subsequent dynamics inside a nanopore by analyzing bubble-induced current-blockage signatures. Once Joule heating was started by triggering a voltage pulse, the liquid temperature inside the nanopore started rising from the ambient temperature. After an initial heating period, a bubble nucleated and grew, blocking the ion flow. During this period, the nucleated bubble first grew under the limiting effect of inertial forces due to the high superheating temperature, followed by heat-transfer-controlled growth where vapor evaporation occurred at the interface. However, due to the limited sensible heat stored in the liquid inside the nanopore, the evaporation soon ceased, and condensation began. This triggered the bubble collapse, as the vapor pressure was not sufficient to overcome the Laplace pressure. The entire duration covering bubble nucleation, growth, and collapse constituted one downward current spike. Following the bubble collapse, both ion flow and Joule heating resumed until a second bubble nucleated, repeating the cycle. Successive bubble nucleation and reheating led to transient current spikes.

A. Early hetero nucleation

Figure 7 shows the bubble generation characteristics of a $D_p = 525$ nm pore under bias voltages of (i) 6.36 V, (ii) 6.45 V, and (iii) 7.08 V. Note that the current signals can be nonidentical for each experimental configuration. We examined the bubble generation repeatedly (Supplemental Material, Sec. 6 [15]), and this revealed two different waiting times t_{nuc} before the first bubble

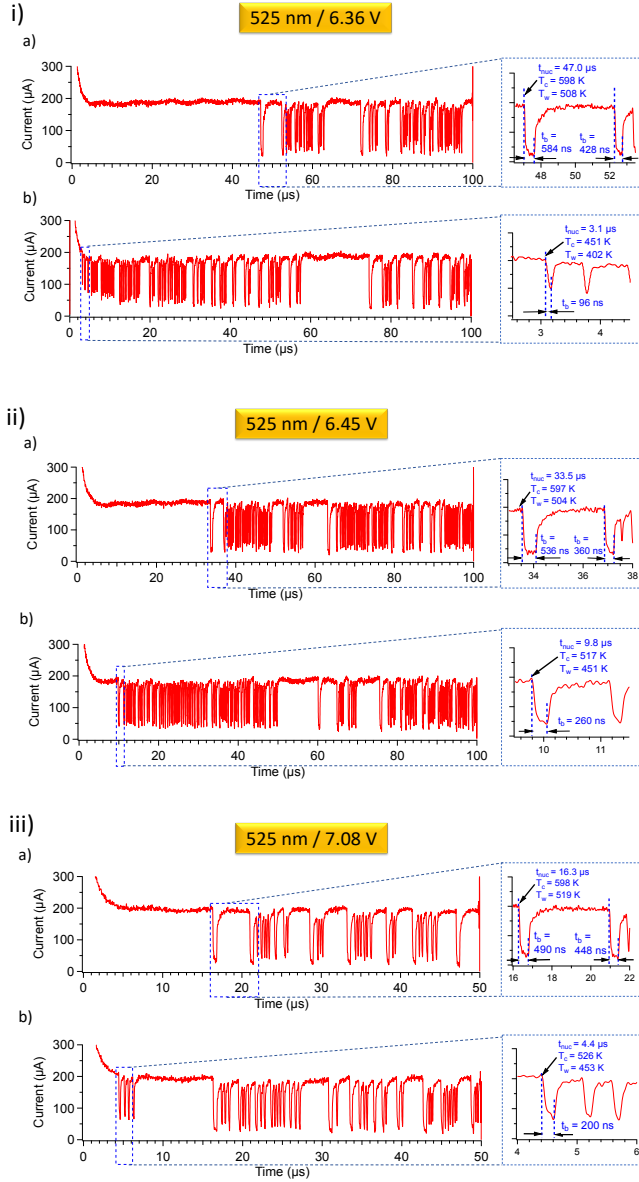


FIG. 7. (i) 6.36 V, (ii) 6.45 V, and (iii) 7.08 V across a 525-nm pore. (a) Bubble signal* sequence for the dominant case starting with a homo nucleation followed by a mixture of homo and hetero bubble modes. (b) Bubble signal* sequence for the rare case of early hetero nucleation. (*Current data captured at 2.5 GS/s, sampled at 250 MHz and filtered at 25 MHz using an eighth-order Butterworth filter).

was detected. For a majority of the pulses [Case (a)], the first bubble appeared after a long waiting time (47 μ s, 33.5 μ s, and 16.3 μ s for 6.36 V, 6.45 V, and 7.08 V, respectively), while in rare occurrences [Case (b)] bubble generation started much earlier ($t_{nuc} = 3.1 \mu$ s, 9.8 μ s, and 4.4 μ s for 6.36 V, 6.45 V, and 7.08 V, respectively). Note that for the 6.45-V bias, early hetero nucleation was also observed at 6.9 μ s, as shown in the Supplemental Material, Fig. S6.2 [15]. We estimated the transient varia-

tion of the pore-center temperature T_c and the pore-wall temperature T_w through Joule-heating simulations for all pore configurations under study (Supplemental Material, Fig. S4.1 [15]). For Case (a), the nucleation happened as long as T_c reached 597 K–598 K. As the kinetic limit for homo nucleation ($\sim 575 \text{ K}$) was exceeded, it can be concluded that the bubble was formed from the pore center. On the other hand, for Case (b), T_c was 451 K, 517 K, and 526 K, respectively, for the three voltages [Fig. 7(b)], much lower than the kinetic limit of homo nucleation. It is reasonable to infer that they were hetero bubbles nucleating on the pore walls. With regard to these early hetero nucleation events, two questions arise: i) what were the conditions leading to their occurrence and ii) why, in most cases, was it suspended? To clarify this,

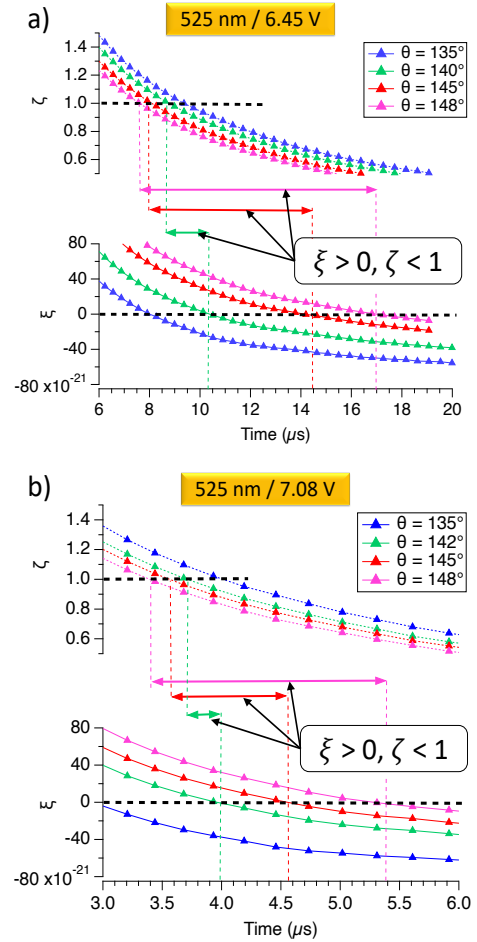


FIG. 8. Transient variation of ξ (solid lines) and ζ (dotted lines) for bias voltages of (a) 6.45 V and (b) 7.08 V across a 525-nm pore.

we calculated ξ [Eq. (22)] and ζ [Eq. (13)], as seen in Fig. 8. At the early stages of superheating, $\xi > 0$; however, as the Joule heating progressed, more Joule heat was liberated at the pore center, causing ΔT_p to rise. Consequently, the specific free energy for homo cluster group formation decreased at a higher rate than for the

hetero group. Eventually, homo cluster formation becomes more favorable, i.e., $\xi < 0$. For successful hetero nucleation, the necessary condition of $\zeta < 1$ must be satisfied before the limit of $\xi = 0$ is reached. As Joule heating progresses, r^* is reduced for a given $\theta > 90^\circ$ according to Eq. (6), and thus ζ also decreases [Eq. (13)]. Also, ζ decreases with θ [Eq. (13)], as a_i decreases with θ when $\theta > 90^\circ$. Meanwhile, ξ increases with θ , as the minimum work for hetero cluster formation decreases, as per Eq. (16) and Fig. 4. Therefore, only when θ exceeds a certain value ($\sim 140^\circ$ – 142° in Fig. 8) does there exist a time period during which the necessary conditions for hetero nucleation are satisfied (i.e., $\xi > 0$ and $\zeta < 1$).

We summarize these valid periods in Fig. 8, which are marked by arrows. It is shown that the period shrinks with the decrease of θ . For $\theta = 135^\circ$, the two conditions are never satisfied simultaneously. Note that the early hetero nucleation points, $t_{\text{nuc}} = 9.8 \mu\text{s}$ in Fig. 7(ii)(b) and $t_{\text{nuc}} = 4.4 \mu\text{s}$ in Fig. 7(iii)(b), agree with the predicted periods at $\theta = 140^\circ$ in Fig. 8(a) and $\theta = 145^\circ$ in Fig. 8(b), respectively. After four early hetero bubbles in Fig. 7(iii)(b), nucleation ceased until a homo bubble appeared at $16.3 \mu\text{s}$, consistent with our analysis that the hetero cluster formation is suppressed due to the decrease of ξ with time. As the period for hetero transition enlarges with θ [Fig. 8], the early hetero nucleation should be able to last much longer as θ increases. However, spontaneous hetero bubble growth at high θ is highly unfavorable because the additional free-energy barrier W_{he}^{**} due to contact-line pinning increases. As a result, for $\theta > 148^\circ$ nanobubbles may nucleate on the pore surface, but they do not grow and have virtually no effect on the nanopore current and thus no blockage signals are registered for them during sensing experiments. Based on previous studies, the static θ on a piranha-cleaned silicon nitride surface should be in the range 20° – 60° [31]. Our results indicate that when the metastability is sufficiently high, in rare situations, a hetero nucleus can form at non-equilibrium θ . A similar observation was reported in a previous study [32], where, due to high supersaturation on a geometrically constrained nanoelectrode, bubble nucleation at an out-of-equilibrium θ of 150° was recorded for a platinum surface.

B. Hetero nucleation during reheating

Intriguingly, after nucleation of the first bubble, subsequent bubble events were observed, as shown in Fig. 7. However, neither the blockage duration nor the waiting times separating two bubbles were uniform (as shown in Fig. 7). To understand the root cause behind this non-periodicity, we performed statistical analysis of these signals. An in-house bubble-signal analysis package was developed in MATLAB [33] to identify the blockage duration of each bubble event and the waiting time preceding it. Figures 9(a) and 9(b) show histograms of the blockage duration for bubble events recorded at 6.36 V and

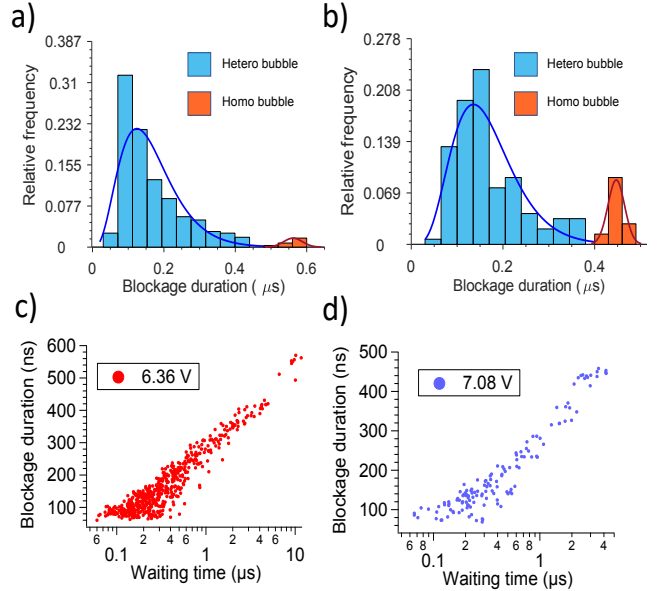


FIG. 9. Histogram of bubble blockage duration for bias voltages of (a) 6.36 V and (b) 7.08 V across a 525-nm pore. Two peaks were identified, implying two modes of bubble generation. The lower peak covered high blockage-duration homo bubbles (orange bars) while the higher peak covered short-duration hetero bubbles (blue bars). Panels (c) and (d) show scatter plots of blockage duration versus waiting time for successive bubbles formed after the first homo bubble for 6.36 V and 7.08 V, respectively.

7.08 V for multiple pulse signals (Supplemental Material, Figs. S6.1 and S6.3 [15]).

Two clear peaks are identified. The smaller peak (orange bars) covers high blockage-duration bubble events while the larger peak (blue bars) demonstrates shorter blockage-duration bubbles. From the scatter plots in Figs. 9(c) and 9(d), we find that the blockage duration of successive bubbles is proportional to the waiting time preceding its nucleation. A longer waiting time allowed more storage of sensible heat in the liquid, enabling the bubble to grow to a bigger size and thus resulting in a longer current blockage. It is also shown that the majority of bubbles had a waiting time less than $1 \mu\text{s}$. As there is a strict cutoff temperature of $\sim 575 \text{ K}$ for homo nucleation, these early nucleation events during the reheating sequence are suspected to be from the pore walls. Due to the lower amount of sensible heat in the liquid at the nucleation point, these hetero bubbles were small and collapsed quickly (indicated by the blue bars) compared with the homo bubbles (indicated by the orange bars).

The higher prevalence of hetero bubbles during reheating can be traced back to a lower value of ΔT_p . After the bubble collapses, the liquid inside the nanopore retains a part of the thermal energy and the post-collapse nanopore temperature is higher than the ambient temperature (Supplemental Material, Fig. S7.1(a) [15]). As a result, the Joule heating rate is higher during the re-

heating sequence and the rise of temperature back to nucleation conditions will be faster. Actually, the average post-collapse temperature within the pore volume increases with decreasing pore size. A smaller pore generates smaller bubbles, which spread out the stored sensible heat in the liquid prior to nucleation over a smaller area. As a result, the average temperature inside the pore post-collapse is usually higher for a smaller pore. According to our simulations, the average pore temperatures for the first homo bubble post-collapse for the 525-nm pore under 7.08 V and the 280-nm pore under 6.84 V were 335 K and 353 K, respectively. A higher collapse temperature implies two outcomes: i) less Joule heat is needed to return to nucleation temperature, ii) the Joule heating rate is higher as electrical conductivity increases with temperature, allowing more current to flow through the nanopore, and the subsequent waiting times are reduced as a result. For the 107-nm pore used in the previous study by Golovchenko’s group [4, 5], the waiting time observed was 117 ns, while for the 525-nm pore and the 280-nm pore, the waiting times between the first two successive homo bubbles were recorded to be 4.18 μ s [Fig. 7(iii)(a)] and 1.36 μ s [Fig. 11(a)], respectively. Due to the reduction in waiting time, ΔT_p is reduced during the reheating period compared to the initial heating period for a given pore and voltage configuration according to Eq. (3). Consequently, the probability of hetero nucleation increases.

In most cases, when the first bubble nucleates homogeneously after a long initial waiting time, the second bubble also nucleates homogeneously after a much shorter waiting time. This trend becomes more dominant as the lifetime of the first bubble increases. For example, in Fig. 7(iii)(a), the lifetime of the first bubble is 490 ns, while the lifetime of the second bubble is 448 ns. According to the histograms in Fig. 9(b), both these bubbles fall within the homo bubble blockage-duration range. As the second homo bubble is short lived, the post-collapse temperature would be higher than that of the first bubble, increasing the probability of hetero nucleation after the second bubble as compared to after the first bubble. Furthermore, as the hetero bubbles are smaller and shorter lived, the post-collapse temperature is expected to be higher, thereby lowering the waiting time, and the accumulated ΔT_p at the next nucleation point will be lower, which makes the hetero transition easier. Thus, once hetero bubble nucleation starts during reheating, it becomes difficult to revert back to the homo nucleation mode. As a result, the fraction of bubbles nucleating heterogeneously is considerably higher than the fraction nucleating homogeneously [Figs. 9(a) and 9(b)].

Compared to the 7.08-V bias, the fraction of homo bubbles is smaller for the 6.36-V bias, as a lower H enables a lower value of ΔT_p . As a result, hetero transition becomes comparably more predominant during the reheating sequence. This phenomenon is captured in Figs. 9(a) and 9(b), where the fraction of hetero bubbles is larger than the fraction of homo bubbles by a greater

margin for the 6.36-V bias than the 7.08-V bias.

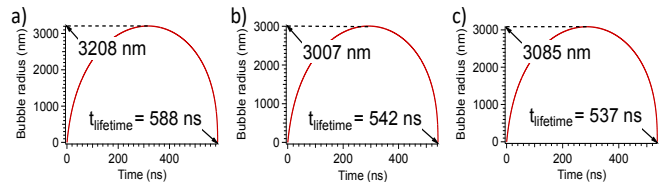


FIG. 10. Panels (a), (b), and (c) show the simulated bubble growth and collapse for the first homo bubble nucleating at t_{nuc} in Fig. 7(a) for 6.36 V, 6.45 V, and 7.08 V, respectively across a 525-nm pore.

Bubble growth and collapse was simulated by solving the Rayleigh–Plesset equation over a moving-boundary one-dimensional liquid mesh [34]. Details of the governing equations are provided in the Supplemental Material, Sec. 8 [15]. In this method, we assumed spherical bubble dynamics and the liquid temperature distribution to be symmetric along the bubble circumference. Moreover, heat dissipation through the membrane walls was neglected, which resulted in a slight overestimation of the sensible heat available in the liquid during growth. The bubble lifetime in the simulations therefore slightly overpredicts the blockage duration seen in the experiments. Figures 10(a), 10(b), and 10(c) show the simulated bubble growth and collapse for the first homo bubble in Figs. 7(i)(a), 7(ii)(a), and 7(iii)(a), respectively. Compared to the experimentally observed blockage durations of 584 ns, 536 ns, and 490 ns, the simulated lifetimes were 588 ns, 542 ns, and 537 ns, respectively. Compared to the 7.08-V homo bubble, the 6.36-V homo bubble grows to a larger size and survives for a longer time because a lower heating rate results in a larger waiting time, thus storing more sensible heat in the liquid. This is the same reason behind the shift of the homo bubble peak towards the higher blockage-duration range in the 6.36-V histogram compared to the 7.08-V histogram. The strong correlations among the waiting times, available sensible heat, and bubble lifetime are also demonstrated for hetero bubbles. The early hetero bubble observed at 3.1 μ s in Fig. 7(i)(a) (inset) has a shorter lifetime (96 ns) than the 260-ns hetero bubble observed at 9.8 μ s in Fig. 7(ii)(a) (inset). Also, compared to this 260-ns bubble, the early hetero bubble at 4.4 μ s in Fig. 7(iii)(a) (inset) has a shorter duration of 200 ns. In this case, although the T_w is almost similar, the higher waiting time for the 6.45-V bubble allows more sensible heat to be stored in the liquid, resulting in longer-duration bubbles.

To validate the simulation results, we refer to the nanobubble collapse time t_c model [35], which was obtained by adding a surface tension term to Rayleigh’s macrobubble collapse formula [36, 37]. The original ‘Rayleigh collapse’ formula was derived through numerical integration of the Rayleigh–Plesset equation, neglect-

ing thermal, viscous, and capillary effects:

$$t_c = 0.915 \left(\frac{\rho R_{\max}^2}{P + 2\gamma/R_{\max} - P_v} \right)^{\frac{1}{2}}. \quad (23)$$

The maximum bubble radius reached in Fig. 10(c) is $R_{\max} = 3085$ nm. At this point, $\dot{R} = 0$, but the bubble interface is under a net compressive force as the vapor pressure P_v is lower than the Laplace pressure. This triggers its collapse. The vapor pressure inside the bubble and the surface tension of the interface were calculated for the interface temperature of 338 K attained at $R = R_{\max}$, which remained almost constant for the majority of the collapse duration. According to Eq. (23), the estimated collapse time is 256 ns, which is in good agreement with the simulated collapse time (252 ns). This validates the numerical scheme of bubble dynamics followed in this paper.

C. Quasi-periodic signals for a 280-nm pore

Figure 11(a) shows the bubble signals for a 280-nm diameter pore under a bias voltage of 6.84 V. For this voltage, multi-pulse signal analysis reveals that bubble generation started consistently at $14.8 \pm 0.3 \mu\text{s}$ at $T_c = 587$ K (Supplemental Material, Figs. S6.4 and S4.1(d) [15]). As this temperature is greater than the kinetic limit, it is indicated that the bubbles were homo bubbles. The experimental blockage duration was 118 ns [Fig. 11(a)], while the simulated bubble lifetime was 165 ns. This overestimation may be due to the assumptions made in the model. Unlike the 525-nm pore, the rare cases of early hetero nucleation were not observed for the 280-nm pore under a 6.84-V bias. After the first bubble collapsed, the reheating continued for $1.36 \mu\text{s}$ before the nucleation of the second bubble (homo). The repeating of this cycle leads to periodic current-blockage signals of uniform duration and separated by consistent waiting times.

For the multi-pulse bubble signals (Supplemental Material, Fig. S6.4 [15]), we found that for three out of seven pulses, only periodic homo bubbles were observed, while for the remaining four pulses, transitions into non-periodic hetero bubbles were observed after a few homo bubbles. However, in general, periodic homo bubbles were more dominant than hetero bubbles in the 280-nm pore (in contrast to the 525-nm pore). Through ξ - ζ analysis, we investigated why the hetero nucleation was largely suppressed in the 280-nm pore. As seen in Fig. 11(b), which shows the transient variation of ξ and ζ during the initial heating period, the favorable time window for hetero nucleation starts appearing for $\theta = 148^\circ$, which is higher than $\theta = 140^\circ$ for the 525-nm pore. This is caused by the steeper temperature variation in the smaller pore (i.e., a higher ΔT_p), which lowers ξ . As the contact angles of the hetero nuclei increase, the secondary free-energy barrier W_{he}^{**} also increases. As shown in Fig. 5(d), even for the same value of θ , a smaller

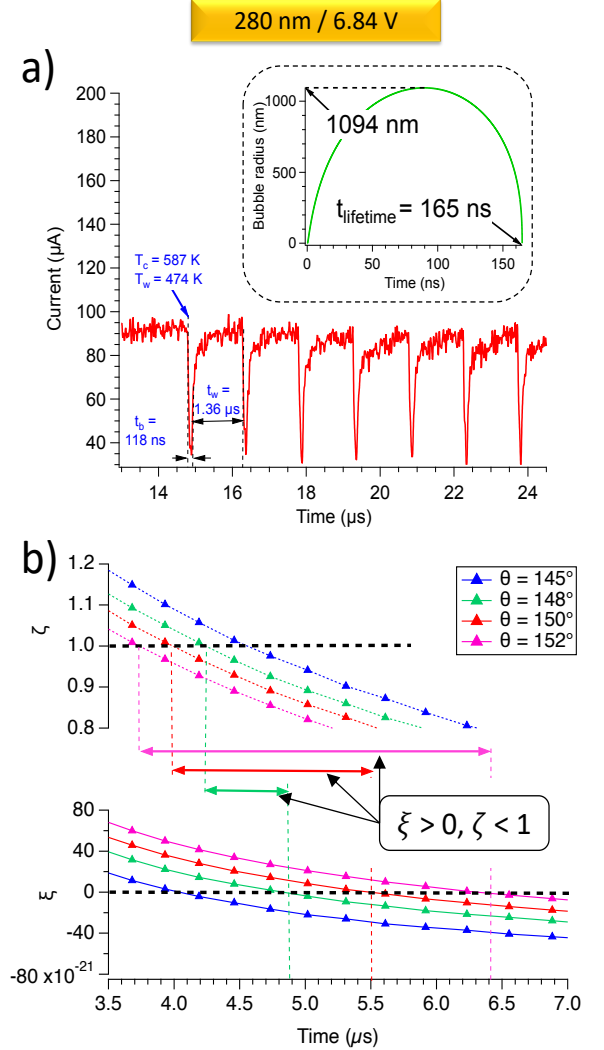


FIG. 11. (a) Bubble signals* and (b) transient variation of ξ (solid lines) and ζ (dotted lines) for $D_p = 280$ nm under a 6.84-V bias. (*Current data captured at 2.5 GS/s, sampled at 500 MHz and filtered at 50 MHz using an eighth-order Butterworth filter.)

pore is associated with a higher value of W_{he}^{**} . From Fig. 5(d), we find that W_{he}^{**} for a $\theta = 148^\circ$ critical cluster inside the 280-nm pore is nearly two times that of a $\theta = 145^\circ$ critical cluster inside the 525-nm pore. Due to the combined effects of pore curvature and higher ΔT_p , the threshold for hetero bubble formation is increased for a smaller pore, making the occurrence of hetero bubbles during the experiments significantly lower.

V. CONCLUSIONS

We showed that nanopore bubble generation is neither always homogeneous nor periodic. The temperature difference between the pore center and its walls, ΔT_p , decides the bubble nucleation at the pore walls. We

show that even if the wall temperature allows the formation of a hetero nucleus, nucleation can be suppressed if $\Delta T_p > 0$. We demonstrate that this behavior can be captured by a new thermodynamic parameter, the transition barrier (ξ), which considers the relative free-energy costs of cluster groups originating at the pore center and the pore walls. When both the necessary conditions of $\xi > 0$ and $\zeta < 1$ are met, hetero nucleation may occur. In addition, we found that growth of pinned hetero nuclei requires overcoming an additional free-energy barrier to reach spontaneous-growth conditions. This made hetero bubbles more prevalent during reheating, when a lower value of ΔT_p allows low-contact-angle hetero nuclei to appear on the pore walls, and these are easy to destabilize. As growth of nucleated nanobubbles is largely fluctuation driven, it is stochastic by nature. However, homo nucleation is kinetically controlled, causing deterministic nucleation temperatures and waiting times. To partially

suppress hetero nucleation, we engineered a pore with a high ΔT_p by reducing the pore diameter to 280 nm. Additionally, it was shown that the secondary energy barrier increases for smaller diameter pores, making growth of pinned hetero surface nanobubbles more difficult. As a result, the 280-nm pore showed quasi-uniform and quasi-periodic generation of homo bubbles.

VI. ACKNOWLEDGMENTS

This work was supported by the Japan Society for the Promotion of Science (JSPS) KAKENHI Grant Numbers 20H02081 and 20J22422. A part of this work was conducted at the Advanced Characterization Nanotechnology Platform of the University of Tokyo, supported by the Nanotechnology Platform of the Ministry of Education, Culture, Sports, Science, and Technology (MEXT), Japan, Grant Number JPMXP09A19UT0167.

-
- [1] J. R. Thome and V. Dupont, Bubble Generator (2007), US Patent 7,261,144.
- [2] G. Liu, J. Xu, and Y. Yang, Seed Bubbles Trigger Boiling Heat Transfer in Silicon Microchannels, *Microfluid. Nanofluidics* **8**, 341 (2010).
- [3] J. Xu, G. Liu, W. Zhang, Q. Li, and B. Wang, Seed Bubbles Stabilize Flow and Heat Transfer in Parallel Microchannels, *Int. J. Multiph. Flow* **35**, 773 (2009).
- [4] G. Nagashima, E. V. Levine, D. P. Hoogerheide, M. M. Burns, and J. A. Golovchenko, Superheating and Homogeneous Single Bubble Nucleation in a Solid-State Nanopore, *Phys. Rev. Lett.* **113**, 24506 (2014).
- [5] E. V. Levine, M. M. Burns, and J. A. Golovchenko, Nanoscale Dynamics of Joule Heating and Bubble Nucleation in a Solid-State Nanopore, *Phys. Rev. E* **93**, 13124 (2016).
- [6] C. Pellow, D. E. Goertz, and G. Zheng, Breaking Free from Vascular Confinement: Status and Prospects for Submicron Ultrasound Contrast Agents, *Wiley Interdiscip. Rev. Nanomed. Nanobiotechnol.* **10**, e1502 (2018).
- [7] M. Fan, D. Tao, R. Honaker, and Z. Luo, Nanobubble Generation and its Application in Froth Flotation (Part I): Nanobubble Generation and its Effects on Properties of Microbubble and Millimeter Scale Bubble Solutions, *Min. Sci. Tech.* **20**, 1 (2010).
- [8] S. Witharana, B. Phillips, S. Strobel, H. D. Kim, T. McKrell, J. B. Chang, J. Buongiorno, K. K. Berggren, L. Chen, and Y. Ding, Bubble Nucleation on Nano- to Micro-Size Cavities and Posts: An Experimental Validation of Classical Theory, *J. Appl. Phys.* **112**, 064904 (2012).
- [9] Y. Wang, M. E. Zaytsev, G. Lajoinie, H. L. The, J. C. T. Eijkel, A. van den Berg, M. Versluis, B. M. Weckhuyzen, X. Zhang, H. J. W. Zandvliet, and D. Lohse, Giant and Explosive Plasmonic Bubbles by Delayed Nucleation, *Proc. Natl. Acad. Sci.* **115**, 7676 (2018).
- [10] E. Boulais, R. Lachaine, and M. Meunier, Plasma-Mediated Nanocavitation and Photothermal Effects in Ultrafast Laser Irradiation of Gold Nanorods in Water, *J. Phys. Chem. C* **117**, 9386 (2013).
- [11] M. T. Carlson, A. J. Green, and H. H. Richardson, Superheating Water by CW Excitation of Gold Nanodots, *Nano Lett.* **12**, 1534 (2012).
- [12] E. Y. Lukianova-Hleb, X. Ren, R. R. Sawant, X. Wu, V. P. Torchilin, and D. O. Lapotko, On-Demand Intracellular Amplification of Chemoradiation with Cancer-Specific Plasmonic Nanobubbles, *Nat. Med.* **20**, 778 (2014).
- [13] S. Baral, A. J. Green, M. Y. Livshits, A. O. Govorov, and H. H. Richardson, Comparison of Vapor Formation of Water at the Solid/Water Interface to Colloidal Solutions Using Optically Excited Gold Nanostructures, *ACS Nano* **8**, 1439 (2014).
- [14] O. Neumann, A. S. Urban, J. Day, S. Lal, P. Nordlander, and N. J. Halas, Solar Vapor Generation Enabled by Nanoparticles, *ACS Nano* **7**, 42 (2012).
- [15] See Supplemental Material at <https://doi.org/10.1021/acs.nano.9b09964> for further information.
- [16] Y.-C. Chou, P. Masih Das, D. S. Monos, and M. Drndić, Lifetime and Stability of Silicon Nitride Nanopores and Nanopore Arrays for Ionic Measurements, *ACS Nano* **14**, 6715 (2020), pMID: 32275381, <https://doi.org/10.1021/acs.nano.9b09964>.
- [17] D. M. Nguyen, L. Hu, J. Miao, and C.-D. Ohl, Oscillate Boiling from Electrical Microheaters, *Phys. Rev. Appl.* **10**, 044064 (2018).
- [18] J. Li, G. Peterson, and P. Cheng, Dynamic Characteristics of Transient Boiling on a Square Platinum Microheater Under Millisecond Pulsed Heating, *Int. J. Heat Mass Transf.* **51**, 273 (2008).
- [19] Z. Yin, A. Prosperetti, and J. Kim, Bubble Growth on an Impulsively Powered Microheater, *Int. J. Heat Mass Transf.* **47**, 1053 (2004).
- [20] C. T. Avedisian, The Homogeneous Nucleation Limits of Liquids, *J. Phys. Chem. Ref. Data* **14**, 695 (1985).
- [21] A. Gadaleta, C. Sempere, S. Gravelle, A. Siria, R. Fulcrand, C. Ybert, and L. Bocquet, Sub-Additive Ionic Transport Across Arrays of Solid-State Nanopores, *Phys.*

- Fluids **26**, 12005 (2014).
- [22] P. G. Debenedetti, *Metastable Liquids: Concepts and Principles* (Princeton University Press, 1996).
- [23] D. Wu, Y.-Y. Duan, and Z. Yang, Thermodynamic Model for Heterogeneous Bubble Nucleation in a Temperature Gradient, *Appl. Phys. Lett.* **97**, 081911 (2010).
- [24] M. Soleimani, R. J. Hill, and T. G. van de Ven, Bubbles and Drops on Curved Surfaces, *Langmuir* **29**, 14168 (2013).
- [25] J. Zou, H. Zhang, Z. Guo, Y. Liu, J. Wei, Y. Huang, and X. Zhang, Surface Nanobubbles Nucleate Liquid Boiling, *Langmuir* **34**, 14096 (2018).
- [26] H. Watanabe, M. Suzuki, H. Inaoka, and N. Ito, Ostwald Ripening in Multiple-Bubble Nuclei, *J. Chem. Phys.* **141**, 234703 (2014).
- [27] J. Marqusee and J. Ross, Theory of Ostwald Ripening: Competitive Growth and its Dependence on Volume Fraction, *J. Chem. Phys.* **80**, 536 (1984).
- [28] Y. De Smet, L. Deriemaeker, and R. Finsy, A Simple Computer Simulation of Ostwald Ripening, *Langmuir* **13**, 6884 (1997).
- [29] Y. Tomo, Q. Y. Li, T. Ikuta, Y. Takata, and K. Takahashi, Unexpected Homogeneous Bubble Nucleation near a Solid-Liquid Interface, *J. Phys. Chem. C* **122**, 28712 (2018).
- [30] E. Tjhung, C. Nardini, and M. E. Cates, Cluster Phases and Bubbly Phase Separation in Active Fluids: Reversal of the Ostwald Process, *Phys. Rev. X* **8**, 031080 (2018).
- [31] L. Barhoumi, A. Baraket, N. M. Nooredeen, M. B. Ali, M. N. Abbas, J. Bausells, and A. Errachid, Silicon Nitride Capacitive Chemical Sensor for Phosphate Ion Detection Based on Copper Phthalocyanine–Acrylate-Polymer, *Electroanalysis* **29**, 1586 (2017).
- [32] S. R. German, M. A. Edwards, H. Ren, and H. S. White, Critical Nuclei Size, Rate, and Activation Energy of H₂ Gas Nucleation, *J. Am. Chem. Soc.* **140**, 4047 (2018).
- [33] MATLAB, *9.6.0.1174912 (R2019a) Update 5* (The MathWorks Inc., Natick, Massachusetts, 2019).
- [34] A. J. Robinson and R. L. Judd, The Dynamics of Spherical Bubble Growth, *Int. J. Heat Mass Transf.* **47**, 5101 (2004).
- [35] F. Magaletti, L. Marino, and C. M. Casciola, Shock Wave Formation in the Collapse of a Vapor Nanobubble, *Phys. Rev. Lett.* **114**, 064501 (2015).
- [36] L. Rayleigh, VIII. On the Pressure Developed in a Liquid During the Collapse of a Spherical Cavity, *Philos. Mag.* **34**, 94 (1917).
- [37] C. E. Brennen, *Cavitation and Bubble Dynamics* (Cambridge University Press, 2014).